Title

Ballistic impact response of an UHMWPE fiber reinforced laminate encasing of an aluminum-alumina hybrid panel

Permalink

https://escholarship.org/uc/item/4x01641t

Authors

O'Masta, MR
Compton, BG
Gamble, EA
et al.

Publication Date

2015-12-01

DOI

10.1016/j.ijimpeng.2015.08.003

Peer reviewed

Ballistic impact response of an UHMWPE fiber reinforced laminate encasing of an aluminum-alumina hybrid panel

CrossMark

M.R. O'Masta [a,*], B.G. Compton [b], E.A. Gamble [b], F.W. Zok [b], V.S. Deshpande [c], H.N.G. Wadley [a]

[a] Department of Material Science & Engineering, School of Engineering and Applied Science, University of Virginia, Charlottesville, VA 22904, USA
[b] Materials Department, University of California, Santa Barbara, CA 93106, USA
[c] Cambridge University Engineering Department, Trumpington Street, Cambridge CB2 1PZ, UK

ABSTRACT

The impact response of an ultrahigh molecular weight polyethylene (UHMWPE) fiber reinforced polymer matrix composite laminate has been investigated. The laminate encapsulated an aluminum alloy sandwich panel whose corrugated core was filled with prismatic alumina inserts. The laminate encased hybrid core target could sustain ceramic prism base impacts by a spherical, 12.7 mm diameter steel projectile with velocities in excess of 2.7 km s^{-1}. This was 150% higher than the ballistic limit of an equal areal density, similarly encapsulated aluminum plate target. By contrast, when the projectile impacted a hybrid core target at the apex of a ceramic prism insert, failure of the UHMWPE laminate on the rear face occurred at a lower impact velocity. High-speed imaging, three-dimensional digital image correlation and x-ray tomography measurements are used to show that upon impact the projectile and the ceramic insert fragment. These fragments then load the UHMWPE laminate on the rear face with a significantly reduced pressure compared to the impact pressure of the projectile on the front surface of the target. The loading area on the inner surface of the rear laminate was highest for a prism base impact and lowest for a prism apex impact. The inability to penetrate the rear laminate of the base impacted samples is consistent with the recent identification of an impact pressure controlled mechanism of progressive penetration in this class of laminate.

© 2015 Elsevier Ltd. All rights reserved.

1. Introduction

Ultra high molecular weight polyethylene (UHMWPE) fiber is one of the highest specific strength materials commercially available today [1], and is used to make ropes, sails, tear and cut resistant fabrics and ballistic impact protection systems. For ballistic applications, 10–20 µm diameter fibers are combined with thermoplastic polymer matrices to form thin (~50 µm thick) unidirectional plies containing ~ 85% by volume fibers. Four of these plies are typically combined to form a cross-ply [0°/90°]$_2$ tape. The tapes can be stacked and hot pressed to form cross-ply [0°/90°]$_n$ laminates that are attached to the rear of an armor system [2,3] or molded to form a protective structure [4].

The transverse impact of such a laminated polymer composite plate by a projectile causes it to deflect out of plane. In a well-designed application, the resulting in-plane membrane stresses create retarding forces on the projectile, eventually bringing it to rest before (elastic) fiber fracture occurs [5]. However, a variety of recent experiments has identified a weaker mechanism of panel response that appears to govern the initial interaction of the projectile with such a target [1,6–10]. A progressive mechanism of penetration is often observed during high velocity impact of edge restrained panels [6,11–15], and it is especially evident when back supported, or very thick panels, are impacted at zero obliquity [1,16–18]. In these cases, the laminates are unable to deflect out of plane, and instead, an impact pressure dependent mode of penetration occurs [12,16,17].

Attwood et al. [19] recently conducted a series of quasi-static compression tests on UHMWPE fiber reinforced composite laminates to investigate their compressive response. They discovered the existence of an indirect tension mode of ply failure when cross-ply laminates were compressed (the mechanism was absent in unidirectional composites). Tension in the fiber direction of each ply was shown to be activated by lateral expansion of the orthogonally oriented plies above and below them; a consequence of the very large anisotropy of the Poisson expansion parallel and transverse to the ply fiber direction. As a result, as [0°/90°]$_n$ laminates are subjected to out of plane compression, the fibers become loaded

* Corresponding author. Department of Material Science & Engineering, School of Engineering and Applied Science, University of Virginia, Charlottesville, VA 22904, USA. Tel.: +1 4349825670; Fax: +1 4349825677.
E-mail address: mro4h@virginia.edu (M.R. O'Masta).

in tension by a shear lag mechanism. When the tensile stress in a ply reaches the ply tensile strength, unstable ply fracture (with large load drops under constant displacement rate loading) occurs. This mode of failure has been observed in a wide variety of commercial polymer fiber reinforced cross-ply laminates, and the critical pressure for ply failure has been shown to be sensitive to the tensile strength of the plies and to the presence of ply defects [20].

During an impact event, a region of compression develops in a laminate under the projectile. The magnitude of this stress scales with impact velocity, as well as with the shape, density and sound speed of the projectile and its angle of impact [21,22]. Karthikeyan and Russell [23] have suggested that penetration is sensitive to this impact induced compressive stress, which is consistent with penetration being controlled by the indirect tensile fracture of a ply's fibers. The work done in failing the ply, thereby advancing the projectile a ply thickness, is supplied by a reduction of the kinetic energy of the projectile, and so as penetration continues, the projectile slows until the pressure it exerts on the laminate becomes insufficient to cause further indirect tension failure. If the intact section of laminate is sufficiently thick, the projectile is then brought to rest by out of plane panel displacement against the forces resisting membrane stretching.

This two mechanism penetration model suggests that any method that reduces the contact pressure applied to the laminate by a projectile should delay the onset of fiber failure to higher impact velocities. Data compiled for several fiber reinforced laminate systems do indeed show that the ballistic limit increases with the ratio of the projectile impact area to projectile mass [24]. Karthikeyan et al. [25] also observed that when edge clamped UHWMPE fiber reinforced Dyneema® HB26, cross-ply laminates were impacted by large cross sectional area (but low density) metal foam projectiles, the indirect tension mechanism could be suppressed, and the impact energies sustained by the laminate were much greater than those for a localized impact by a solid projectile of similar mass [6,25]. In the metal foam impact experiments, the location of failure was also observed to move from the impact site (for solid projectiles) to the grips, and novel gripping strategies that allowed pull-in of the laminate substantially improved the failure impulse threshold.

O'Masta et al. [1] have recently impacted bi-material targets consisting of an aluminum alloy plate wrapped in a (Dyneema® grade HB26) UHWMPE fiber reinforced laminate with a spherical projectile (Fig. 1a). The aluminum plate thickness was chosen to allow tests at the shatter gap threshold for the projectile/alloy combination [26], while the Dyneema® wrapping strategy was used to avoid grip region laminate failure modes. Impact velocity dependent fragmentation of the projectile within the aluminum plate allowed the cross sectional area of the debris exiting the aluminum plate (and therefore loading the inside of the rear laminate) to be systematically varied. This enabled the cross sectional area of the laminate loading to be varied by about a factor of two, and revealed that the penetration resistance of the laminate was significantly increased as the loading area increased (Fig. 1b and c). The study also led to the discovery that out of plane bulging of the aluminum plate, prior to its perforation by the projectile within, caused the rear laminate to be accelerated away from the alloy plate back face before impact by the projectile debris (Fig. 1a). This decreased the velocity difference between the laminate and the projectile, and allowed the laminate to sustain even higher velocity impacts in comparison to cases where the rear laminate was stationary upon impact.

Several studies of the impact of hybrid sandwich panel structures whose cores contained both hard ceramic and ductile metallic materials have revealed interesting opportunities to tune the impact debris spatial distribution, and potentially applying substantial acceleration to the rear face of the structure during an impact event [27–31]. In a recent study of a model aluminum sandwich panel,

(a) Encased aluminum target
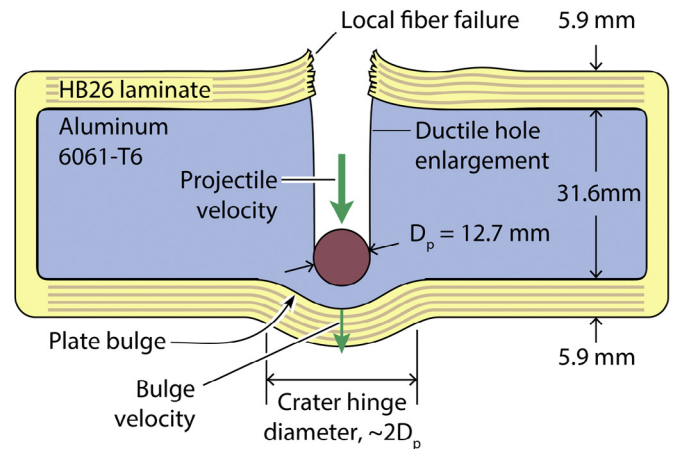
(b) Intact projectile impact
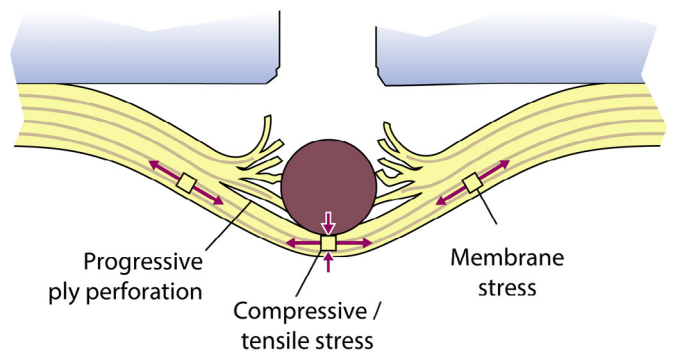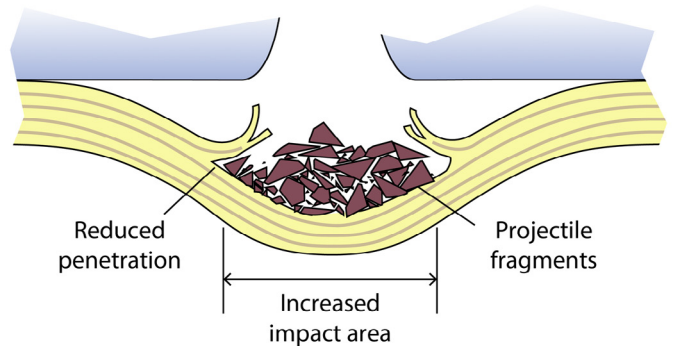

(c) Fragmented projectile impact

Fig. 1. Schematic illustrations of an aluminum plate encased in a (Dyneema® grade HB26) UHWMPE fiber reinforced laminate after impact by a steel sphere. (a) Plate bulging prior to perforation pre-accelerates the rear laminate. The depth of penetration into the laminate upon impact by a projectile that penetrated the plate then depended upon whether the projectile (b) remained intact or (c) had fragmented.

aluminum corrugations were filled with prismatic, triangular cross section alumina inserts, and impacted above either a prism base or a prism apex (Fig. 2) [30]. The rear aluminum face sheet was observed to suffer a large out of plane deflection prior to projectile and target debris ejection. The width of deflected region and debris plume was found to be controlled by the impact location on the front face of the target, and the base width of the corrugated cells, L_c. Impacts above the base of a prism resulted in debris clouds whose width was ~$2L_c$, or four times that of an impacting projectile whose diameter was about 0.5 L_c Fig. 2a. However impacts above a prism

(a) Prism base impact
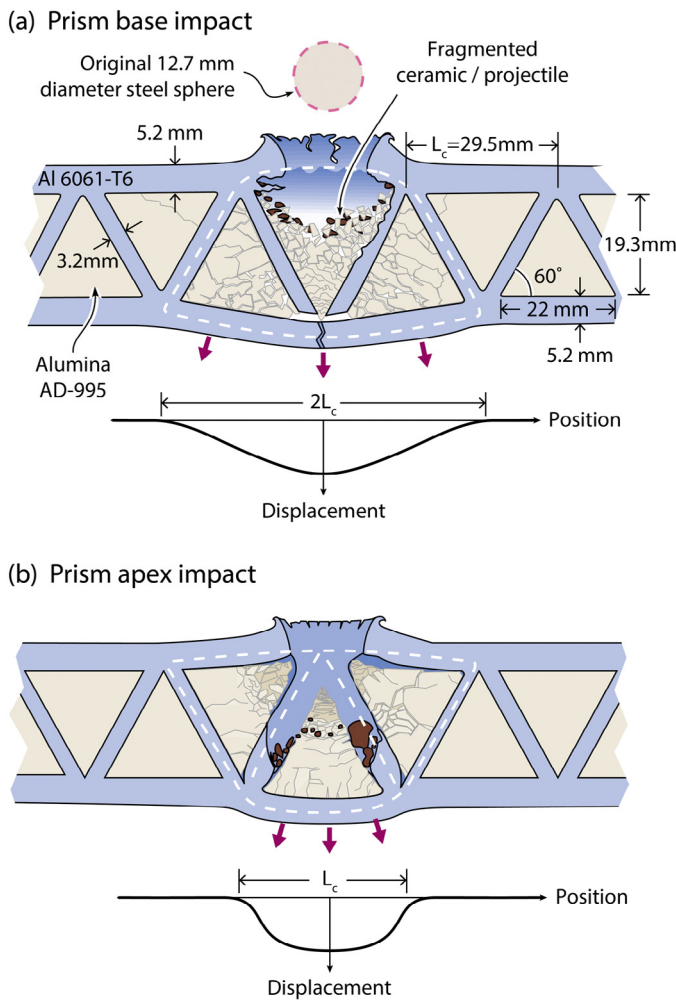

(b) Prism apex impact

Fig. 2. Schematic illustration of a corrugated aluminum sandwich structure with an alumina filled (hybrid) core after impact by a hardened steel sphere. The length of the out of plane displaced region on the rear face depended upon impact location. (a) A ceramic prism base impact resulted in a region of displacement $2L_c$ wide, while (b) shows that an impact at the apex of a prism led to a displacement of half this width.

apex (a corrugation node) (Fig. 2b), resulted in an out of plane deflection width of ~L_c, and with a much increased debris exit velocity.

Repeating such an experiment with a hybrid core test structure encased in a cross-ply UHMWPE fiber reinforced laminate would allow a further assessment of the consequences of changing the rear laminate contact pressure. It will be shown that methods that reduce the contact pressure, and therefore suppress failure by the indirect tension mechanism, substantially increase the penetration resistance of the laminate.

2. Materials and sample fabrication

We probe the effect of encasing hybrid Al/ceramic targets in Dyneema® using two types of target designs: (i) an encased hybrid target as shown in Fig. 3a and b and (ii) the encased target with the rear face cut out as shown in Fig. 3c. The samples were fabricated using the same 5.9 mm thick Dyneema® (DSM; Heerlen, The Netherlands) HB26 fiber-reinforced laminate used in the O'Masta et al. [1] study with solid aluminum plates. The HB26 encased a slightly modified version of the same hybrid core sandwich panel studied by Wadley et al. [30]. In the original Wadley et al. study, the 6061-T6 aluminum alloy sandwich panel had a triangular corrugated core with
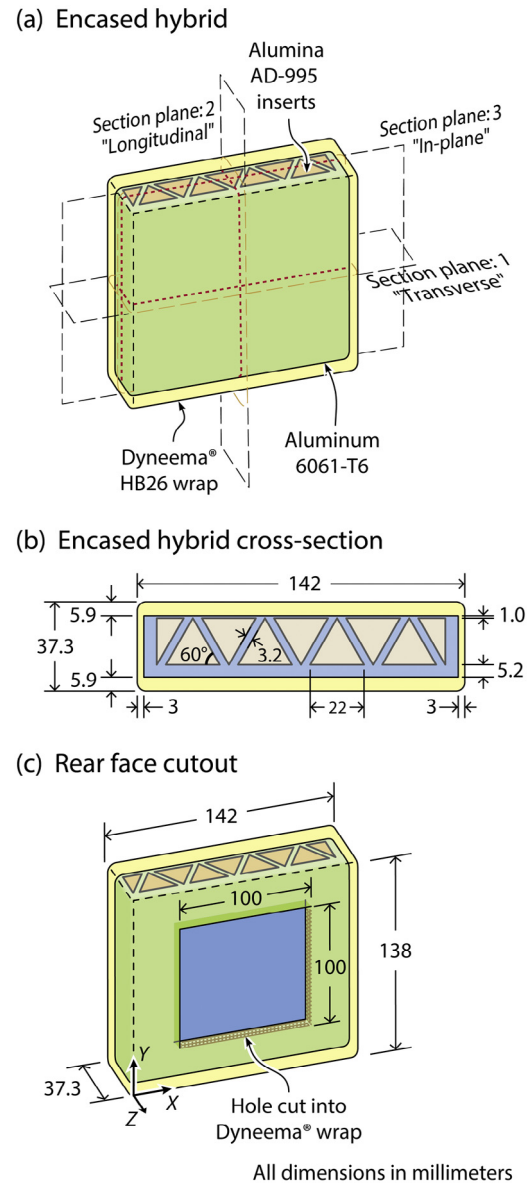
(a) Encased hybrid

(b) Encased hybrid cross-section

(c) Rear face cutout

All dimensions in millimeters

Fig. 3. Schematic illustrations of the two target types investigated in this study. (a) Shows the fully Dyneema® laminate encased sample design with dimensions defined in (b). The sample design with a part of the back laminate removed is shown in (c) together with a coordinate system. Reference planes for subsequent analysis are also shown in (a).

3.2 mm thick webs inclined at an angle of 60° to two, 5.2 mm thick face sheets (Fig. 2). In the present study, the thickness of the face sheet on the impact side of the corrugated panel was reduced to 1.0 mm (Fig. 4a). With this modification, a hybrid core panel with a 5.9 mm thick Dyneema® HB26 laminate encasement had a mass per unit area of $\rho_a = 97$ kg m^{-2}; the same as the original (non-encased) hybrid panel (Fig. 2), and the encased aluminum plate target (Fig. 1).

The model targets were assembled by filling the empty cells of the sandwich panel with CoorsTek (Golden, CO) grade AD-995 triangular prisms that had been coated in Lord (Cary, NC) grade 305 epoxy adhesive (Fig. 4b). This ceramic has a hardness of 14.1 GPa, an elastic modulus of 370 GPa and a fracture toughness of 4–5 MN m$^{-3/2}$. The panels were encased in Dyneema® grade HB26 cross-ply laminate. The HB26 laminate was fabricated from 67 μm thick unidirectional plies made from a polyurethane matrix and 83 vol.% Dyneema® SK76 fiber whose properties have been
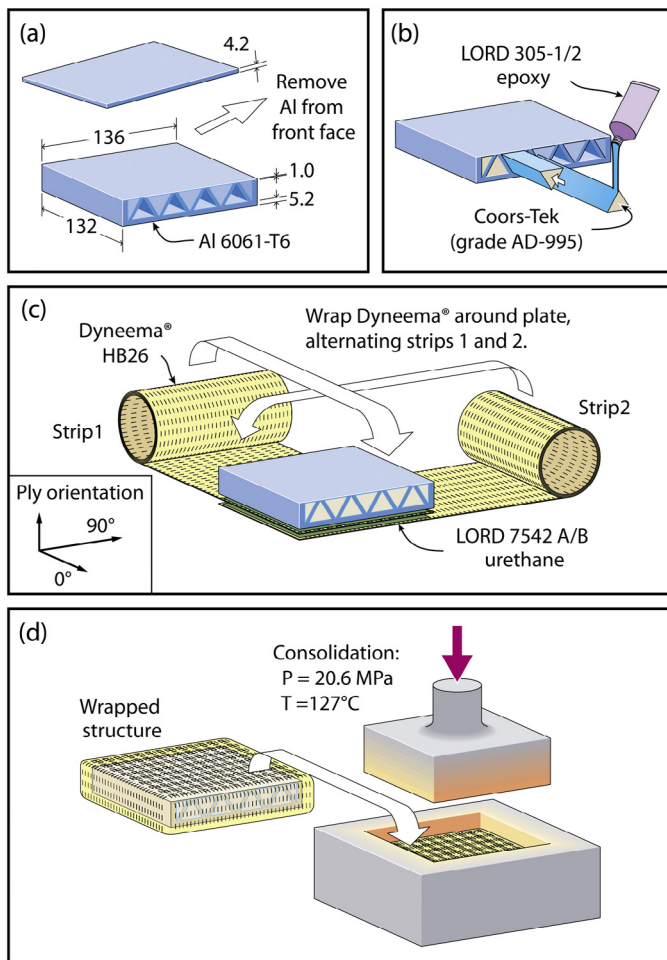
Fig. 4. The fabrication sequence for making the Dyneema® HB26 encased hybrid core panels, whereby (a) the thickness of the Al corrugated panel was reduced, (b) adhesively coated ceramics were inserted into the Al corrugation, (c) the Al/Al₂O₃ (hybrid) panel was encased in a Dyneema® laminate and (d) the laminate was hot-consolidated.

documented elsewhere [1,19,25,32]. Two strips of [0°/90°]₂ HB26 pre-preg tape were alternatively wrapped around the hybrid core panel followed by laminate consolidation at an elevated temperature and pressure (Fig. 4c and d). The lay-up of the laminate on both 136 mm × 132 mm faces was [(90°/0°)₂/(0°/90°)₂]₁₁ with a thickness of 5.9 mm. This was twice the thickness of the four [(0°/90°)]₂₂ sides and was identical to that used for the encased aluminum targets [1]. The length of pre-preg strips was ~5 cm longer than calculated for a perfectly tight wrap. The excess (but densified) Dyneema® accumulated around the periphery of the top (subsequently impacted) surface of the panels. The final dimensions of the encased hybrid target are given in Fig. 3. Fig. 3a also identifies reference planes, while Fig. 3c defines sample external dimensions and a coordinate system used later.

To observe the hybrid sandwich panel's back face deflection, and the debris plume incident upon the inside surface of the rear Dyneema® laminate during an impact event, a central 100 mm × 100 mm square region of Dyneema® was removed using a rotary cutting tool. A speckle pattern was applied to the aluminum surface to enable measurement of the surface displacement of the back surface with a three-dimensional digital image correlation (DIC) system. The exposed aluminum surface was first spray painted white, followed by the application of a stochastic pattern of 1–3 mm diameter black dots that covered approximately 50% of the aluminum surface area.

3. Impact tests and characterization

The same spherical projectile (CCR Products LLC; West Hartford, CT) used in the earlier studies of the encased aluminum plate and the bare hybrid core panel [1,30] was used here. It had a mass of 8.4 g, was 12.7 mm in diameter, and was fabricated from 52100 chrome-steel. Its measured hardness and compressive strength were 7.6 and 3.4 GPa, respectively. Each target was edge clamped, and oriented for 0° obliquity impact either at the mid-span of the 22 mm wide base of the center ceramic prism (Fig. 5), or on the apex of one of the adjacent ceramic prisms. The impact tests on the fully encased hybrid target were performed with a light-gas gun capable of launch velocities up to 3.5 km s⁻¹ located at the University of California, Santa Barbara [31]. The impact velocity, Vi, was measured to within ±0.4% using the time-of-flight recorded between a pair of laser-gates. A model v.7.3 Phantom (Vision Research Inc.; Wayne, NJ) high-speed video camera was oriented normal to the YZ plane, and recorded a backlit profile view of the rear of the sample. The camera recordings used an exposure time of 1 μs and an inter-frame interval of 19.5 μs. After impact, the samples were visually inspected for external damage. Some samples were also examined by x-ray computed tomography (XCT) at Carl Zeiss Imaging (Brighton, MI). All of the samples were then sectioned by water-jet cutting along the transverse plane that intersected the impact sites.

The ballistic impacts of the rear face cutout targets were performed at Chesapeake Testing (Belcamp, MD) where the more open geometry enabled 3D-DIC measurements to be recorded. The impact velocities achievable with this powder gun were limited to Vi < 2.3 km s⁻¹ and were measured using paper break-screens. The Z-component of the residual velocity, Vr, of the leading edge of the debris released from perforated samples was calculated from video images obtained with a model v.1610 Phantom high-speed camera oriented normal to the YZ plane. The recordings used an exposure time of 0.76 μs and an inter-frame interval of 10 μs. A pair of model Fastcam SA-X2 Photron (San Diego, CA) high-speed cameras were positioned in a stereo configuration (α = 17.5°) behind the sample

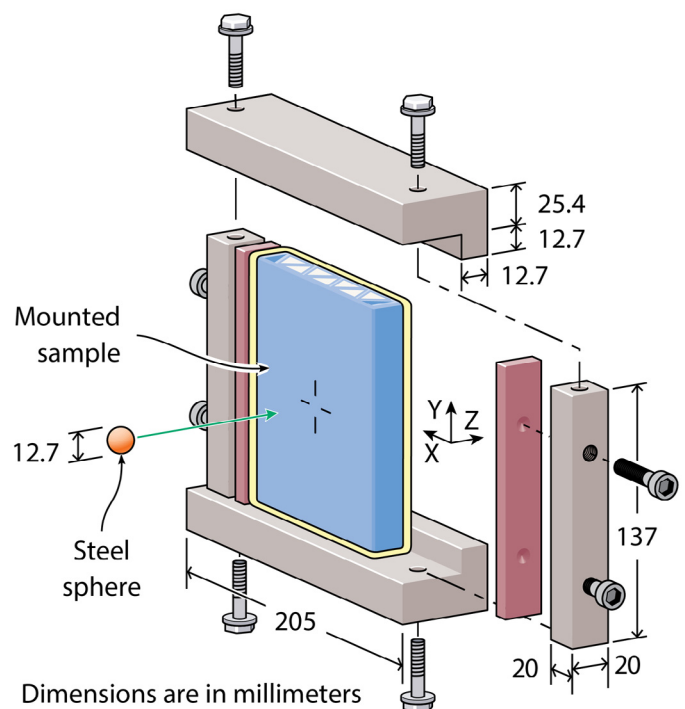**Fig. 5.** Schematic illustration of the ballistic test fixture and sample support configuration.

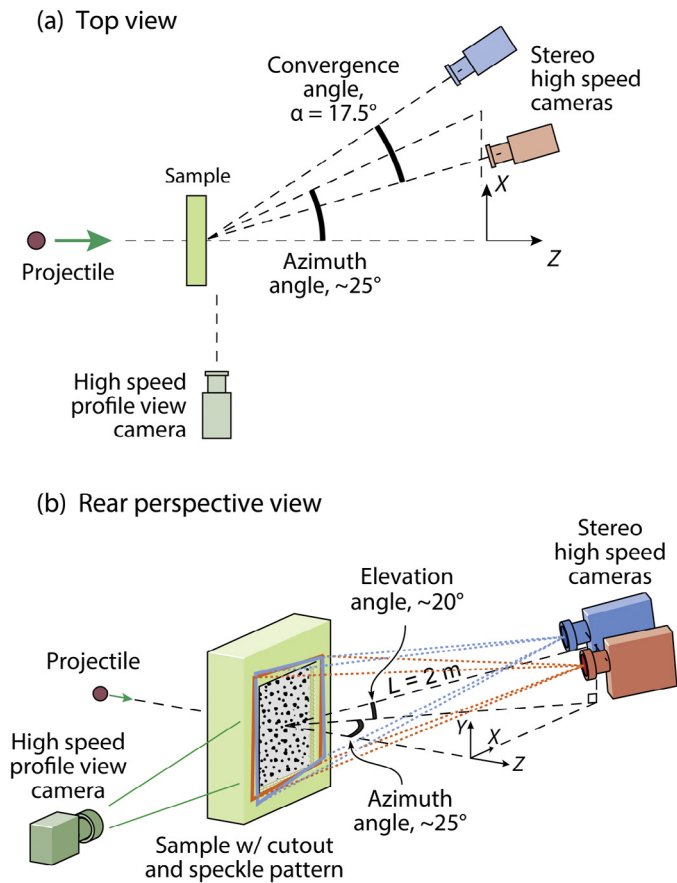## (a) Top view

(b) Rear perspective view

Fig. 6. Schematic illustrations showing (a) the top and (b) the rear perspective views of the impact test geometry used to record 3D DIC measurements.

to record the deflection of the speckle pattern coated rear aluminum surface (Fig. 6). Each black dot filled approximately 6 pixels of a camera's field of view. The cameras were positioned to the side of the Z-axis to avoid damage from debris impact, and were synchronized to capture images at 6.67 μs intervals with an exposure time of 1 μs.

The DIC images were analyzed using the Aramis v.6.3 (GOM mbH; Braunschweig, Germany) 3D image correlation software. This first divided one of the images from the stereo pair into interrogation areas (facets). Each facet was uniquely defined by the speckle pattern encompassed within its 15 pixel × 15 pixel area, and each linear raster of facets was spaced 5 pixels (~1.8 mm) apart. A calibration, using images taken of a NIST-traceable calibration panel (GOM mbH), was used to identify each facet in the second image pair and convert the facet location into the laboratory frame (X, Y, Z) coordinate system. The locations of each facet were recorded for each image pair for the sequence of video images, and the software then calculated the full-field displacements and velocities over the speckled surface as functions of time. Additional details can be found in other studies [33–35].

4. Results

4.1. Encased hybrid targets – ceramic prism base impacts

The majority of the fully encased targets were impacted at a prism base, mid-way along the prism at impact velocities between 0.84 and 2.70 km s^{-1}, while two samples were impacted on a prism apex at velocities of 2.20 and 2.50 km s^{-1}. Table 1 summarizes the impact

Table 1
Impact results for the encased hybrid and rear face cutout targets.

Target type	Impact location	Vi (km s^{-1})	$\dot{\delta}_{max}$ (km s^{-1})	Vr (km s^{-1})
Encased hybrid	Base	0.84	N/R	0
	Base	1.00	N/R	0
	Base	1.34	N/R	0
	Base	1.48	N/R	0
	Base	2.00	N/R	0
	Node	2.20	N/R	0
	Base	2.26	N/R	0
	Base	2.31	N/R	0
	Node	2.50	N/R	0.20
	Base	2.57	N/R	0
	Base	2.70	N/R	0
Rear face cutout	Base	1.71	0.32	0.43
	Base	1.84	0.34	0.50
	Base	1.92	0.35	0.49
	Node	2.00	0.40	0.82
	Node	2.17	0.45	0.80
	Base	2.29	0.45	0.62

N/R: not recorded.

and residual (exit) velocities for these experiments. The projectiles that impacted a prism base were arrested within the samples without ejection of debris, while the Vi = 2.50 km s^{-1} impact on a prism apex resulted in full perforation with a debris exit velocity of 0.2 km s^{-1}. Table 2 summarizes the ballistic limits measured previously for the encased aluminum and the hybrid core reference targets of identical aerial density [1,30]. It is evident that the ballistic limit of the encased hybrid target tested here was near double that of the reference targets.

Transverse cross-sections of several of the encased hybrid core targets impacted at a prism base are shown in Fig. 7. The front (upper) laminate was completely perforated by an impact at 0.84 km s^{-1} (Fig. 7a). This was consistent with a previous measurement of 0.20 km s^{-1} for the ballistic limit of a 5.9 mm thick HB26 laminate supported on a foundation and impacted by the same projectile, Table 3 [1]. The projectile then perforated the 1 mm thick front face sheet and was arrested within the impacted ceramic prism, which suffered substantial comminution. The hole seen in the impacted cell resulted from reverse flow of the comminuted ceramic and projectile fragments through the entry hole during impact together with the loss of the remaining fragments during cross-sectioning. Some microcracking of the two prisms on either side of the impact can also be seen in Fig. 7a. It is interesting to note that the Dyneema® entry hole had partially closed after impact. The target suffered no measureable permanent back face deflection.

The effect of increasing the impact velocity can be seen in Fig. 7b and c. The impact at 1.37 km s^{-1} displaced a wide section of the rear face sheet in the Z-direction, sufficient to cause fracture of the webs of the aluminum corrugated core and the rear face sheet. This resulted in substantial permanent deflection, but no penetration of the rear laminate. The length of the displaced face sheet region was approximately 50 mm, or ~2L$_c$, in the X-direction. XCT results for this sample, (Fig. 8a) show that the length of the displaced face sheet region in the Y-(prism axis) direction was about 75 mm. The position

Table 2
The ballistic limits of reference targets (ρ_a = 97 kg m^{-2}) presented by the highest impact velocity that failed to completely perforate the target and the lowest impact velocity that did.

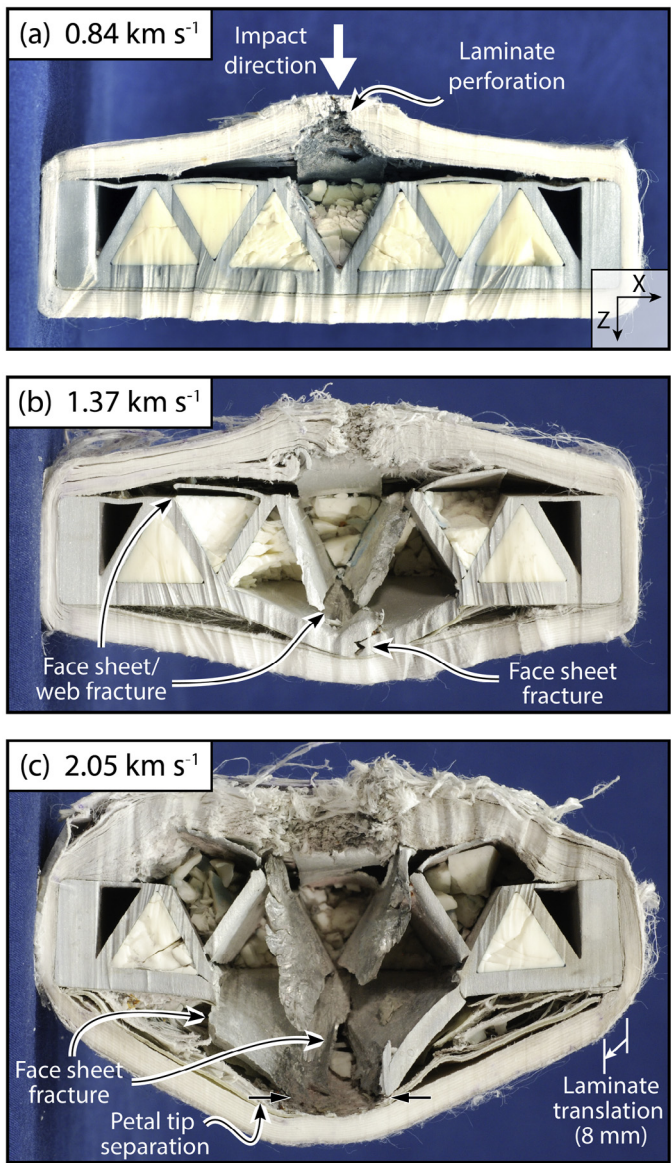| Target type	Impact location	Ballistic limit (km s^{-1})	
		Not perforated	Perforated
Encased Al	Center	1.37	1.41
Hybrid	Base	1.27	1.32
Hybrid	Node	0.98	1.15

Fig. 7. Transverse cross-sections of Dyneema® encased hybrid targets impacted by the 12.7 mm diameter hardened steel sphere on a prism base at impact velocities, Vi, of (a) 0.84, (b) 1.37 and (c) 2.05 km s⁻¹. Wavy vertical lines are an artifact of the water-jet sectioning process.
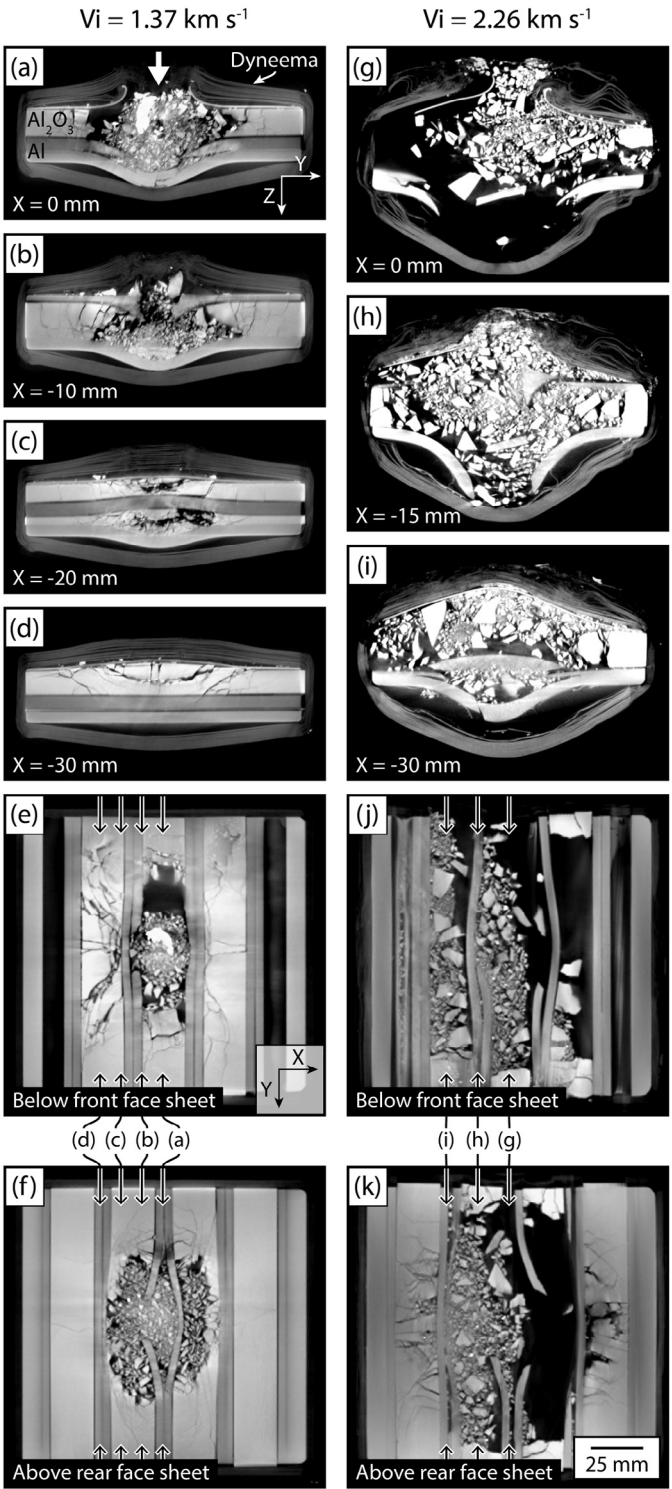

Fig. 8. XCT reconstructions of longitudinal (a–d and g–i) and in-plane (e, f, j and k) cross-sectional renderings of encased hybrid targets impacted at Vi = 1.37 km s⁻¹ (a–f) and Vi = 2.26 km s⁻¹ (g–k). The arrow in (a) indicates impact direction for both samples.

of the hinges about which face sheet deflection occurred, coincided with the base of the cone shaped region of severely microcracked ceramic (Figs. 7b and 8). For impacts with Vi ≥ 1.48 km s⁻¹, the rear face sheet was longitudinally torn directly beneath the impact site and at the two adjacent nodes in the X-direction (Fig. 7c). Fig. 7 also shows that the hole on the front face

increased in width as more substantial reverse debris flow eroded the sides of the entry hole.

The displacement of the rear aluminum face sheet caused a permanent displacement of the rear Dyneema® laminate by a distance that increased with impact velocity (Figs. 7 and 8). At Vi = 2.05 km s⁻¹, rotation of the fractured rear face sheet cut four to six of the

Table 3
The minimum impact velocity for penetration (first ply failure) and perforation (complete laminate failure) of ~5.9 mm thick HB26 laminates when impacted by a 12.7 mm diameter steel sphere.

Target type	Support condition	Velocity (km s⁻¹)	
		Penetration	Perforation
Encased aluminum [1]	Rear supported	<0.11	0.20
Encased aluminum [1]	Edge clamped + pre-acceleration	0.24	0.60
Bare laminate plate [6]	Edge clamped	0.24	0.45

Dyneema® plies and allowed the comminuted ceramic and fragmented projectile debris to impact the laminate. However, this debris impact appears to have caused no additional failure of the rear laminate. The large stretching displacement suffered by the rear laminate appears to have been accommodated by pull-in of plies from the sides and front of the encasement. At the highest test velocity (2.7 km s⁻¹), portions of the laminate encasement at the sides of the sample began to fail (Fig. 9a). No local penetration of the laminate at the impact location was observed in any of the prism base impact experiments.

A high-speed image sequence showing the back face profile of the encased hybrid target impacted at 2.70 km s⁻¹ is shown in Fig. 10. At t = 15 μs,[1] the laminate on the rear of the sample had been displaced 12 mm in the Z-direction and formed a 58 mm wide bulge in the Y-direction, consistent with acceleration by a bulging rear aluminum face sheet. The initial out of plane (Z-component) velocity was 0.5 km s⁻¹, and the distance of the laminate's Z- component deflection increased with time as the aluminum face sheet was fractured and released debris against the laminate. The laminate deflection was accommodated by transverse hinges that propagated away from the impact site with a Y-component velocity of 0.32 ± 0.03 km s⁻¹, identical to that measured for encased aluminum samples. The finger-like protrusions visible at t ≥ 171 μs were delaminated X-oriented fibers that had failed at a side grip. The side edge of the outermost tape strip is highlighted in the t = 366 μs image. This edge feature was a result of the combined pull-in and tensile rupture of laminate material, as previously shown in Fig. 9a. The impact was arrested within 600 μs, after a maximum out of plane deflection of 82 mm.

4.2. Encased hybrid targets – ceramic prism apex impacts

A cross-sectional view of the encased hybrid core target impacted at the apex of a ceramic prism at Vi = 2.50 km s⁻¹ is shown in Fig. 9b. Like a base impact at this impact velocity, the rear laminate transversely deflected, pulled material in from the sides and portions failed in tension along the sides of the sample. However, in the apex impact case, the laminate was perforated below the impact site leaving a ~10 mm diameter hole (Fig. 9c).

4.3. Rear face cutout targets – ceramic prism base impacts

The rear face cutout targets were impacted at a prism base at velocities of 1.71 to 2.29 km s⁻¹ (Table 1). As with the encased hybrid targets, the projectile first perforated the front laminate and the thin aluminum front face sheet followed by fragmentation against the base of the center ceramic prism and activation of hybrid core failure mechanisms. For the 1.71 km s⁻¹ impact, the high-speed video image sequence from one of the oblique rear view cameras of the speckle coated rear face sheet is shown in Fig. 11a. A contour map of the out of plane (Z-component) velocity, $\dot{\delta}$, determined from DIC analysis is overlaid. At t = 4 μs, a small bulge formed on the rear face sheet. Longitudinal and transverse displacement profiles across the peak of the bulge revealed it was longer in the longitudinal direction (Y-axis) than the transverse direction (X-axis) (Fig. 12a and b). The dimensions of the bulge and its velocity increased with time, and a Y-oriented tear in the face sheet[2] started to develop below the node of the centrally impacted cell by t = 24 μs when the peak deflection reached about 6 mm. Ejecta then exited from the tear, as seen in the last frame of Fig. 11a, and from the profile view of the impact in Fig. 11b. The plume of debris had a blunt front and was ~44 mm wide in
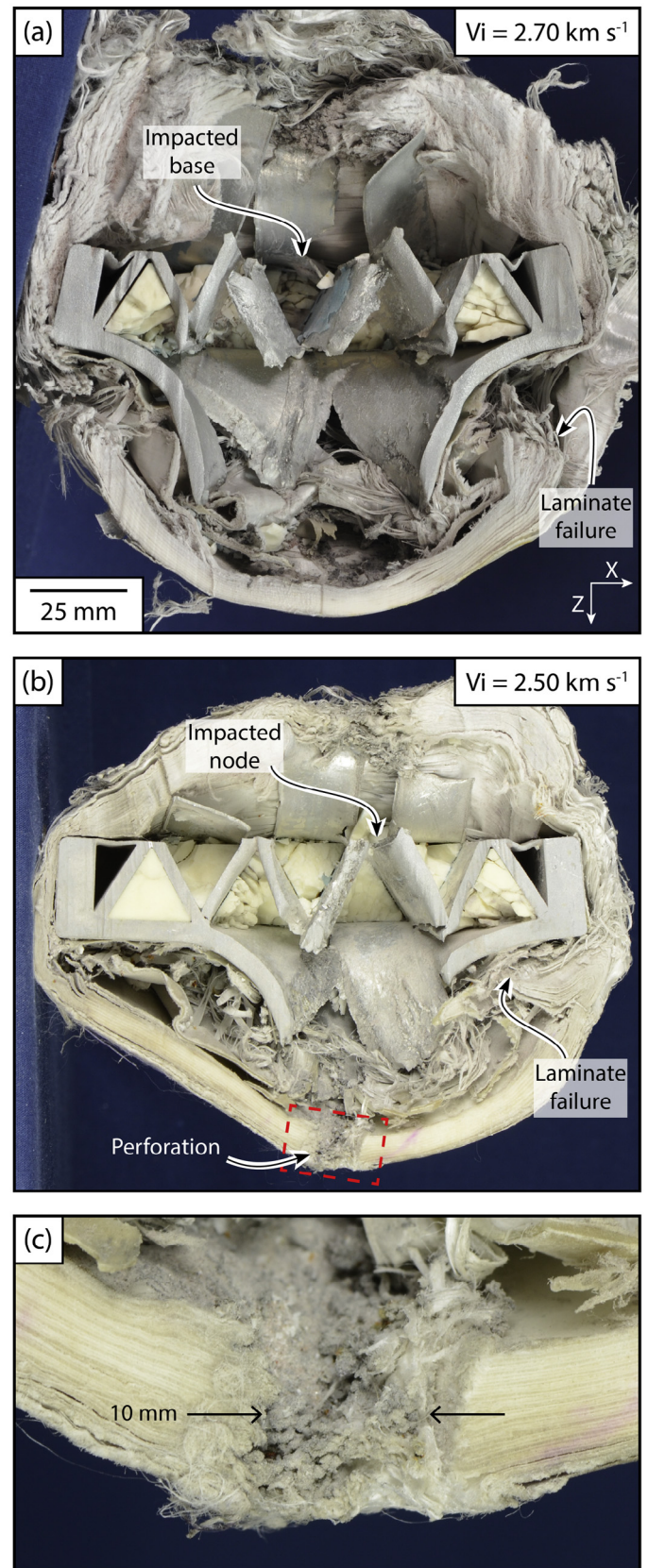

Fig. 9. Transverse cross-sections of encased hybrid targets impacted at either (a) a prism base or (b) a prism apex. Prominent laminate failure mechanisms are identified. (c) Shows a magnified view of the perforated region of the laminate identified in (b).

---

[1] Time $t = 0 \pm 4$ μs was the estimated time of the start of deflection.

[2] DIC facets were not resolved along a tear since the fracture surface changed the identifying "pattern" within a facet's interrogation area.
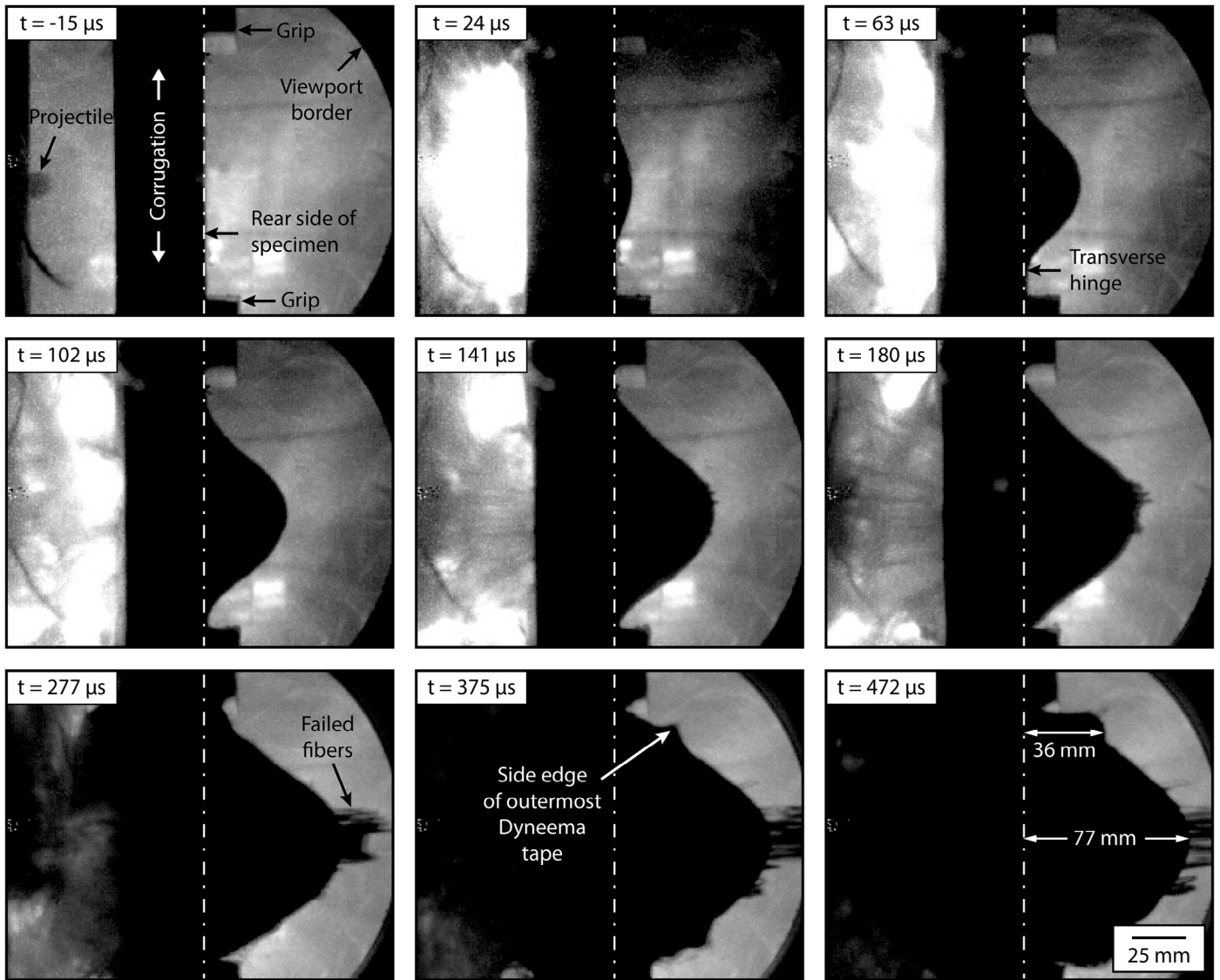
Fig. 10. High-speed video image sequence of an encased hybrid target during prism base impact at Vi = 2.70 km s⁻¹.

the Y-direction, which is consistent with the dimension of the face sheet tear opening (Figs. 8 and 12b), and the dynamic rear laminate deflection profile (Fig. 10). At the fastest tested impact velocity, Vi = 2.29 km s⁻¹, the shape of the bulge along the longitudinal plane was similar to the lower impact velocity, but the transverse profile was more localized (Fig. 12c and d).

The DIC determined velocity at the most deflected location, $\dot{\delta}_{peak}$, is plotted in Fig. 13 as a function of time for the two impact velocities. For the 1.71 km s⁻¹ impact, the rear face sheet accelerated to a maximum deflection rate $\dot{\delta}_{max} = 0.30$ km s⁻¹ at t = 17 μs. The 2.29 km s⁻¹ impact required a similar time to reach $\dot{\delta}_{max} = 0.45$ km s⁻¹. In general, $\dot{\delta}_{max}$ monotonically increased with impact velocity (Fig. 14), as did the terminal debris velocity (increasing from Vr = 0.43 km s⁻¹ to 0.62 km s⁻¹). While the values of Vr were near or above the perforation limit of the laminate when impacted by an intact sphere (Table 3), the difference between $\dot{\delta}_{max}$ and the faster traveling debris, Vr, was only 0.1 to 0.2 km s⁻¹ across the test velocity range. A laminate attached to the rear face sheet would therefore have been pre-accelerated by the motion of the large area face sheet bulge, which would have reduced the debris impact velocity in the laminate frame of reference.

4.4. Rear face cutout targets – ceramic prism apex impacts

A high-speed video image sequence of the speckle coated rear face sheet of a rear face cutout target impact at a prism apex is shown in Fig. 15. Two bulges were initially observed at t = 4 μs. The bulges occurred at the two corrugated web – face sheet nodes on either side of the base of the apex impacted ceramic prism. The peaks merged into one bulge with a 20 mm wide transverse front by t = 10 μs (Fig. 16). Two Y-oriented cracks formed by t = 30 μs and allowed the portion of the rear face sheet under the impacted prism to be subsequently torn away, facilitating release of the debris (Fig. 15). The out of plane velocity at the location of peak deflection, $\dot{\delta}_{peak}$, was shown as a function of time in Fig. 13. The response was similar to those of the base impacts. However, the residual velocity, Vr = 0.8 km s⁻¹, of the debris in this case was substantially higher than the residual velocity for a prism base impact and about 0.4 km s⁻¹ faster than the back face sheet maximum velocity prior to debris emission (Fig. 14). Thus, the rear face sheet of a sample impacted at a prism apex bulged at a similar out of plane velocity to a prism base impact; but the released debris after face sheet failure traveled at more than twice

(a) Oblique rear view with velocity overlay
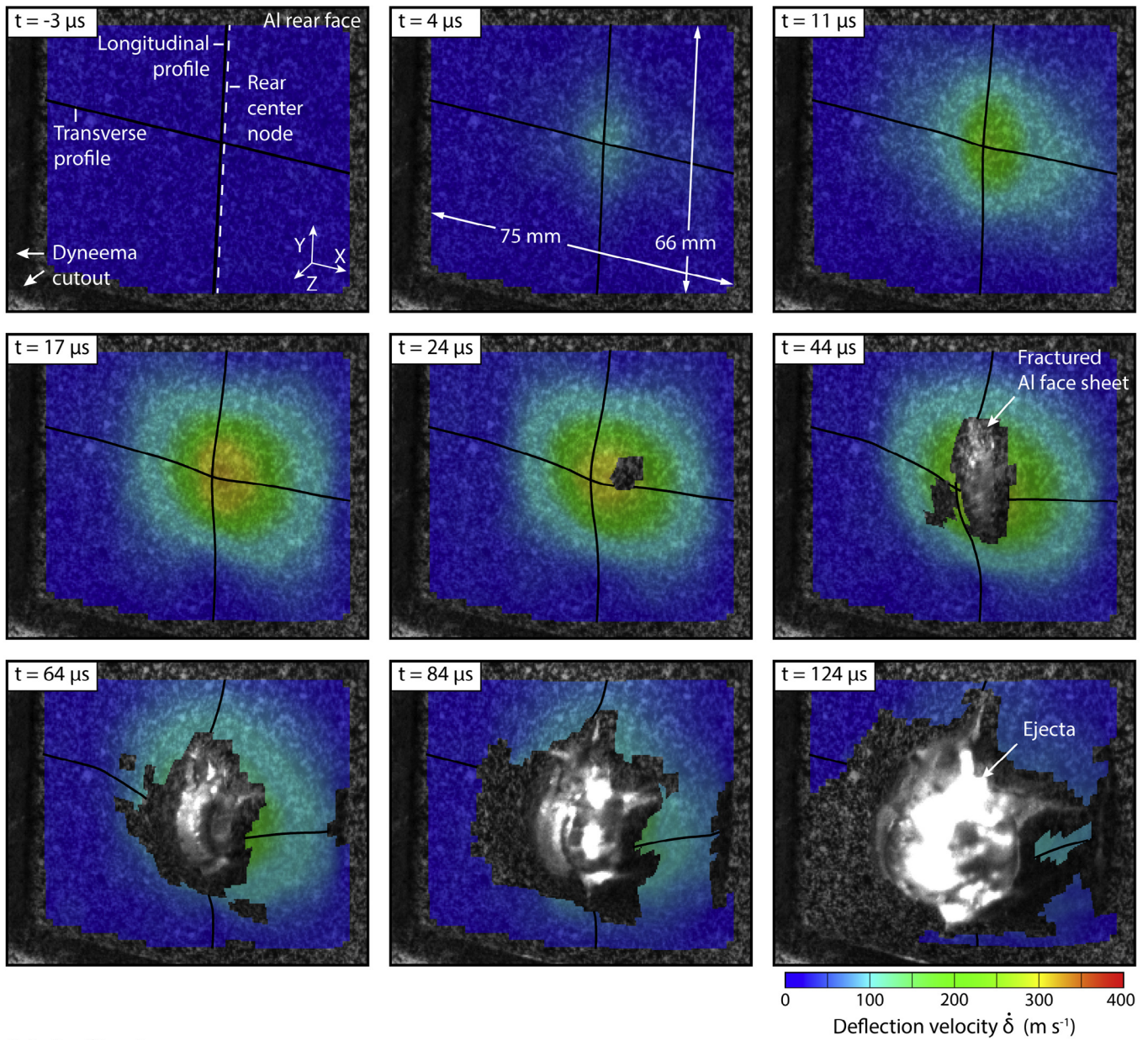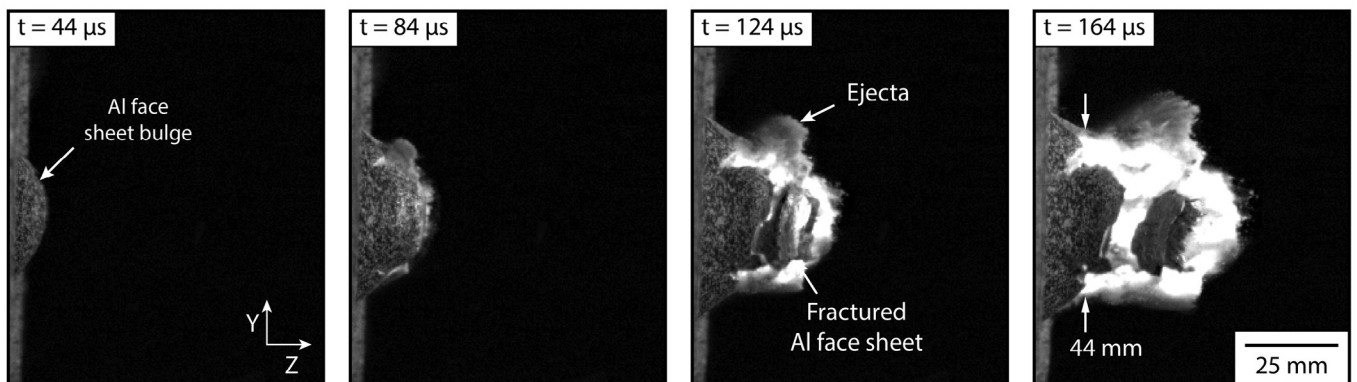

(b) Profile view

Fig. 11. (a) High-speed video image sequence showing an oblique rear view of the back aluminum surface of a rear cutout target that was prism base impacted at $V_i = 1.71$ km s^{-1}. A map of the out of plane surface velocity, $\dot{\delta}$, determined from DIC measurements is superimposed. (b) High speed video images showing the out of plane deflection during sample impact.
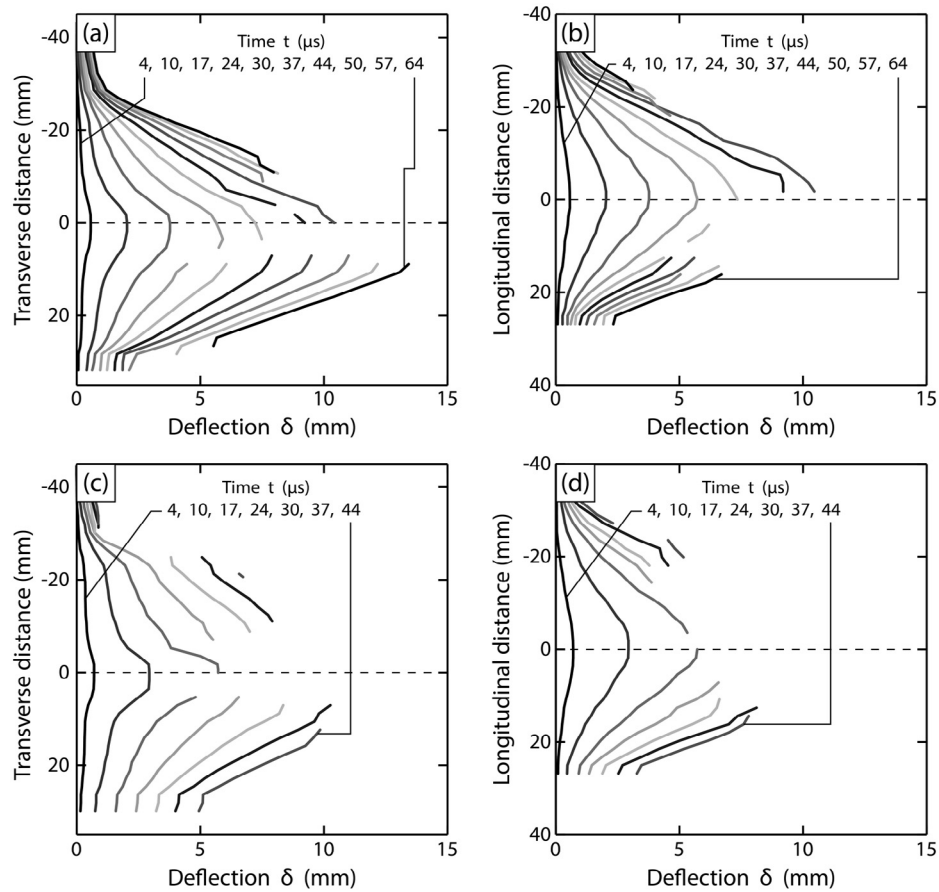
Fig. 12. The out of plane deflection history along (a) transverse and (b) longitudinal profile coordinates, as identified in Fig. 11a, for the rear face cutout target prism base impacted at Vi = 1.71 km s⁻¹. Analogous data for a sample impacted at Vi = 2.29 km s⁻¹ are shown in (c) and (d).
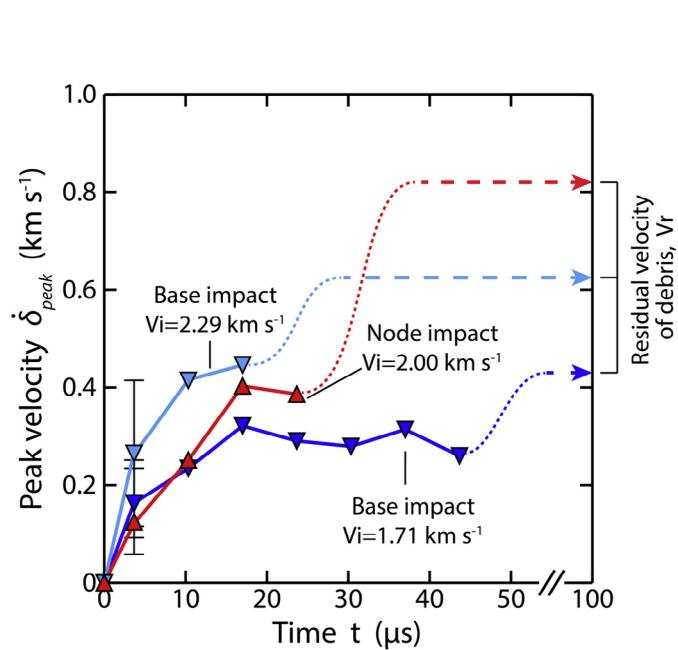

Fig. 13. The peak out of plane velocity, $\dot{\delta}_{peak}$, versus time for rear face cutout targets. Two of the samples were impacted at a prism base and the third at a prism node. The terminal residual velocities after perforation are also shown.
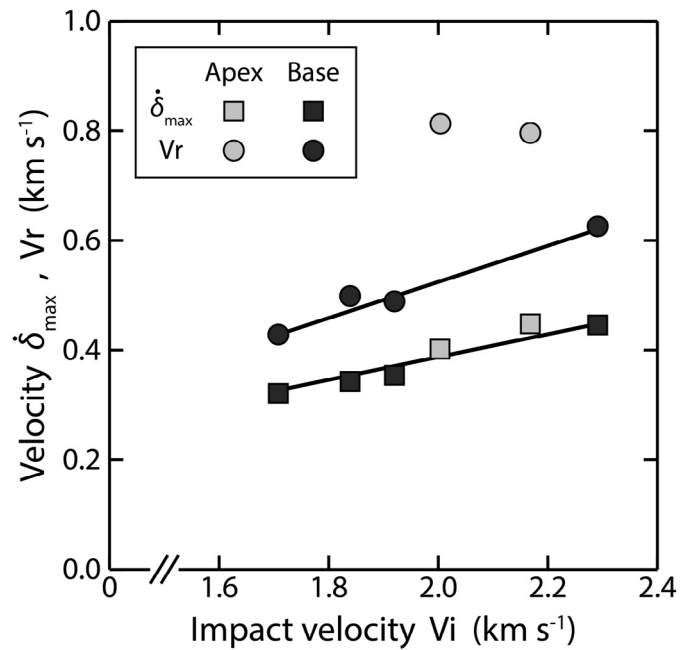
Fig. 14. The debris residual velocity, Vr, and maximum out of plane velocity, $\dot{\delta}_{max}$, of rear face cutout targets versus impact velocity, Vi, for both prism base (dark gray) and prism apex (light gray) impact locations.
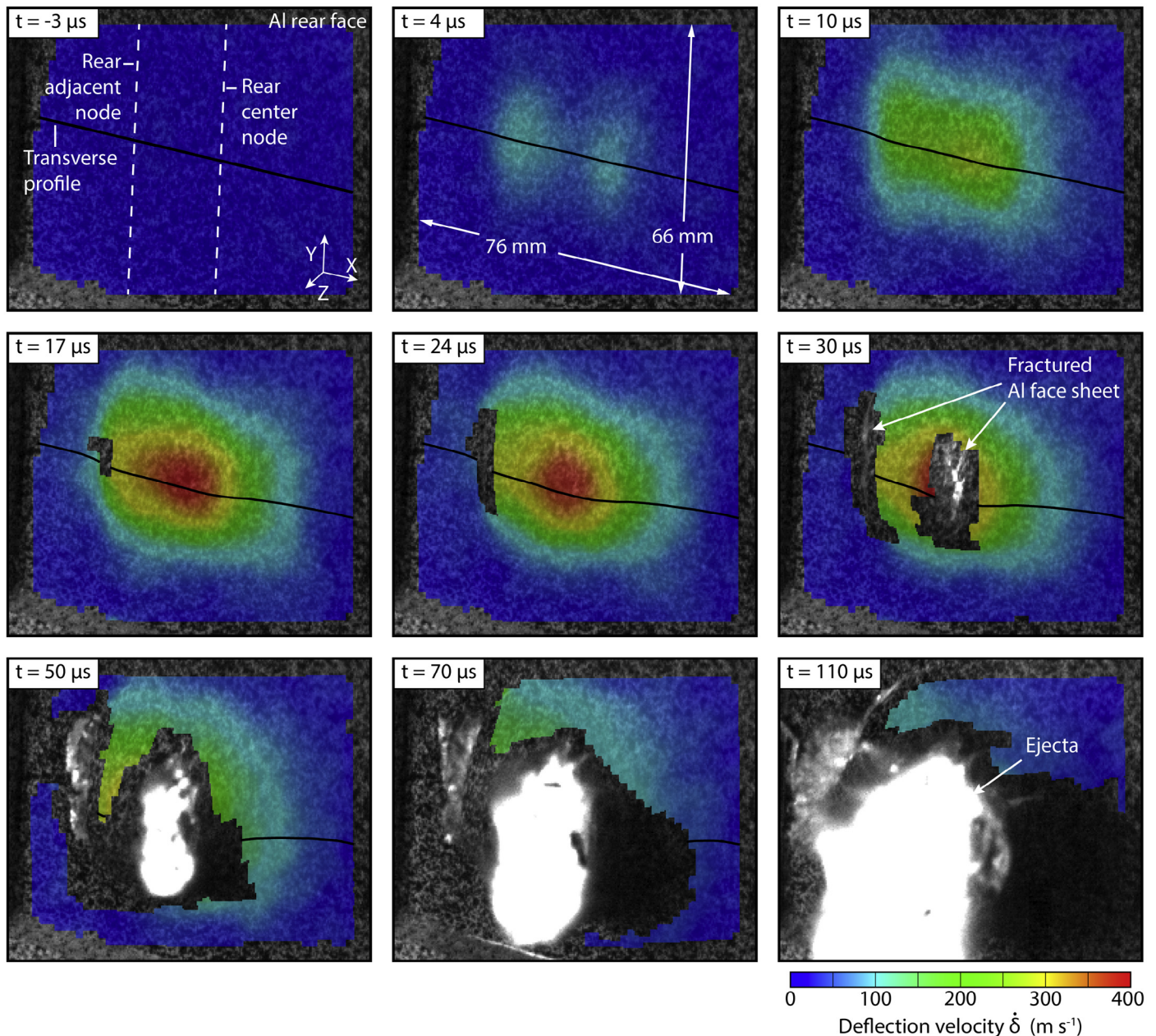
Fig. 15. High-speed video image sequence of the aluminum surface of a rear face cutout target impacted at $V_i = 2.00$ km s^{-1} on a prism apex. A map of the DIC generated out of plane velocity, $\dot{\delta}$, component is superimposed.

the speed as that for a prism base impact at similar incident velocity.

5. Discussion

By impacting a model alumina filled hybrid sandwich panel at either a ceramic prism base or apex, it has been possible to modify the dynamic loading of a rear, 5.9 mm thick Dyneema® laminate. A previous study [1] has shown that the front (back supported) Dyneema® laminate of an encased aluminum plate impacted by the same, 12.7 mm diameter spherical steel projectile, was perforated once the impact velocity exceeded 0.2 km s^{-1} (Table 3). We therefore assume that the projectile velocity that penetrated the front laminate and struck the 1 mm thick front aluminum face sheet did so with an impact velocity reduced by 0.2 km s^{-1}. This velocity was sufficient to perforate the aluminum face sheet and impact either

the 22 mm wide base of the center ceramic prism or the apex of one of the adjacent prisms. The high hardness (14.1 GPa) and elastic stiffness (370 GPa) of the alumina resulted in sufficiently high contact pressures during impact to cause projectile fragmentation at the prism interface. The low fracture toughness of the alumina (4–5 MN m$^{-3/2}$) resulted in the formation of a mescal zone of highly comminuted and pulverized ceramic under the projectile impact site. Cone and radial cracks readily form in alumina tiles [36], but these were disrupted here by the discontinuous nature of the prisms and the ductile aluminum webs. Nevertheless, as the impact velocity increased, the volume of damaged ceramic material increased. Since there was no ceramic disruption along the axis of the prisms, distance of damaged ceramic was greater along the corrugation direction (Y-axis) than transverse to it (X-axis).

The impulse applied to the rear Dyneema® laminate by the fragmented ceramic and projectile debris plume depended upon the
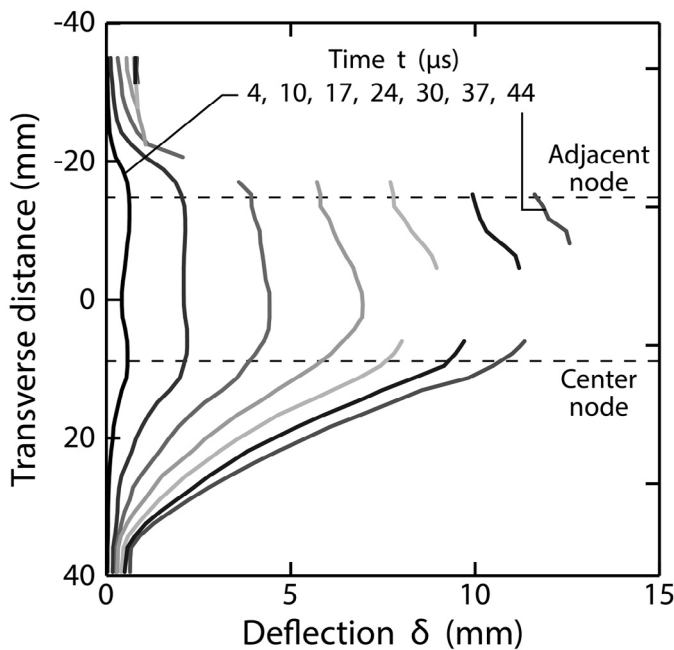
Fig. 16. The temporal evolution of the deflection profile of a rear face cutout target impacted at a prism apex with a velocity of $V_i = 2.00$ km s^{-1}.

site of impact. Impacts at a prism base resulted in a 50 mm wide square shaped region of the rear face sheet being displaced out of plane (Z-direction). After exceeding a displacement of 10 mm, debris was ejected from the fractured rear aluminum face sheet as a more than 40 mm wide plume, with a velocity that increased from 0.43 to 0.62 km s^{-1} as the target incident velocity increased from 1.7 to 2.3 km s^{-1} (Fig. 14). The greatly reduced debris velocity in comparison to the projectile incident velocity is attributed to the large volume (mass) of fragmented ceramic (approximately three prism cross sections) (Fig. 8), over which the projectile momentum was distributed, and the effectiveness, at lower impact velocities, of the front laminate at limiting reverse ejecta flow (and application of its reaction momentum). However, it is still remarkable that impacts at velocities as high as 2.7 km s^{-1} failed to rupture the rear Dyneema® laminate behind the location of debris impact.

A rationale for the response of the base impacted targets is shown schematically in Fig. 17. The pressure applied by the debris was highest at the bottom (apex node) of the impacted cell causing the node and face sheet to fail in tension at the face sheet/node interface (Fig. 17a). The ductile aluminum face sheet then began to bend about plastic hinges that propagated to the left and right until arrest at the two adjacent nodes. Figs. 7b and 17a show that this accelerated a region of face sheet with a width given by ~$2L_c$ outwards reaching a maximum out of plane velocity that increased with impact velocity (Fig. 14). This in turn accelerated the rear Dyneema® laminate with a force that was distributed over a similarly large area. Fig. 13 shows that for the target impacted at 2.3 km s^{-1}, the rear face sheet required approximately 10 μs to reach a velocity of 0.45 km s^{-1}. This was sufficient time for the 5.9 mm thick laminate (with a Z-direction longitudinal wave speed of slightly more than 2 km s^{-1} [21] and transverse hinge speed of about 0.3 km s^{-1}) to transversely deflect, and maintain the impact pressure below the threshold needed to induce indirect tension mode of progressive ply failure. At higher target impact velocities, the faces of the fractured face sheet at the bottom apex node separated, and then released the debris plume to impact the inside of the rear laminate over a region with a width given of ~ $1.5L_c$ (Fig. 17b). While the velocity of the debris over the test range could have been traveling in excess of 0.6 km s^{-1}, the velocity difference between the debris and

slower traveling aluminum face sheet was less than 0.2 km s^{-1} (Fig. 14). The Z-component motion of the face sheet provided a mechanism to reduce the velocity of the impacting debris in the laminate frame of reference. This limited the debris impact pressure, and ensured that it did not exceed the (typically 1.5 GPa) pressure required to activate the indirect tension mode of failure.

This observation is consistent with the behavior of the encased aluminum target, where an impact by the same spherical projectile caused the rear face of the aluminum plate to bulge (with an area limited to ~2× the projectile diameter) prior to plate perforation (Fig. 1a). This resulted in a small pre-acceleration of the rear 5.9 mm thick HB26 laminate which was then impacted by an intact projectile that exited the rear of the aluminum plate with a velocity of 0.6 km s^{-1} which exceeded the ballistic limit of a 5.9 mm thick, stationary, edge clamped Dyneema® laminate impacted by this projectile (Table 3). The indirect tension activation pressure (a property intrinsic to the laminate) remains the same in the pre-accelerated and stationary impact situations; only the impact velocity (and hence contact pressure) applied to the laminate in the pre-accelerated case was lower. Interestingly, impacts at a velocity of only 0.24 km s^{-1} are sufficient to start progressive indirect tensile failure (Table 3). The lack of any penetration in the encased hybrid target can be understood by considering the pressure applied to the laminate by a plume of debris particles scales as ρV_i^2, where ρ is the plume density. The steel projectile is many times more dense than that of the plume of aluminum, alumina and fragmented debris. This, combined with the lower velocity of the debris plume and greater pre-acceleration applied to the laminate, resulted in i) an increase in penetration initiation velocity of the rear laminate from 0.2 km s^{-1} to more than 0.6 km s^{-1} in the laboratory frame of reference, and ii) an increase in ballistic limit of the target from 1.4 km s^{-1} for the Dyneema® encased aluminum plate sample to more than 2.7 km s^{-1} for the prism base impacted sample (of the same areal density).

Debris penetration of the rear Dyneema® laminate after a prism apex impact can also be rationalized by a similar analysis. The impact again displaced the rear aluminum face sheet outward, at a velocity similar to that of a base prism impact, and therefore pre-accelerated the rear Dyneema® laminate to a similar Z-direction velocity (Fig. 17d). In an apex impact, however, the mass of comminuted ceramic was significantly less (Fig. 17c), and the momentum transferred to it by the projectile therefore resulted in a higher debris velocity [30]. For a target impacted at 2 km s^{-1}, the velocity difference between the debris and rear aluminum face sheet was approximately 0.4 km s^{-1} for a ceramic prism node but only 0.1 km s^{-1} for a base impact (Fig. 14). It is expected that the debris impact velocity in the laminate frame of reference would have continued to increase with target impact velocity, and the higher pressure that was applied to the laminate resulted in perforation for the 2.5 km s^{-1} prism apex impact.

In cases where the debris plume that exited the rear of the aluminum sandwich panel was captured by the rear Dyneema® laminate, its kinetic energy could be dissipated by membrane stretching of the full thickness of the rear laminate. Pull-in from the side and front laminates, and straightening of excess consolidated Dyneema® combined to a give larger Z-direction displacement than would have been possible if a side supported rear face laminate (i.e. a typical bolted spall shield) had been impacted, and this presumably enabled kinetic energy dissipation at reduced membrane stress. While no back laminate failure was observed for any of the prism base impacts, some tensile fracture at the sides of the samples impacted at the highest velocity was observed. This was not unexpected since the number of fibers aligned with the tensile load at the sides of the sample was only a half that of the back laminate. This mode of response, as well as deflection behavior, is similar to that observed when beams of the same laminate were impacted by low-density aluminum foam projectiles [25].
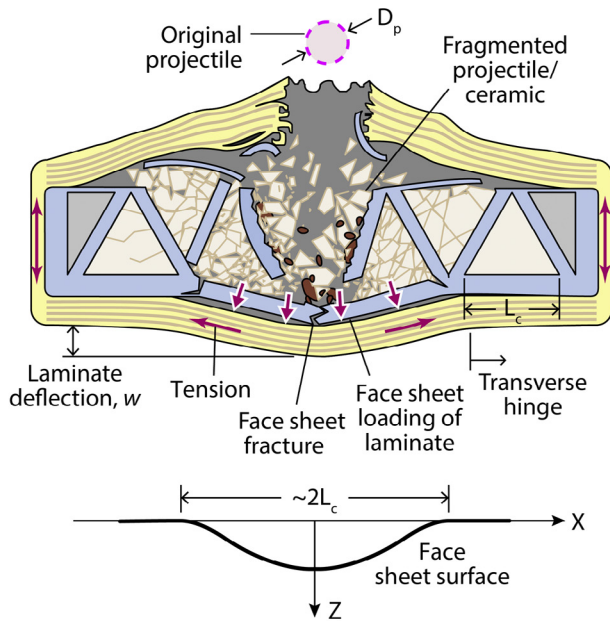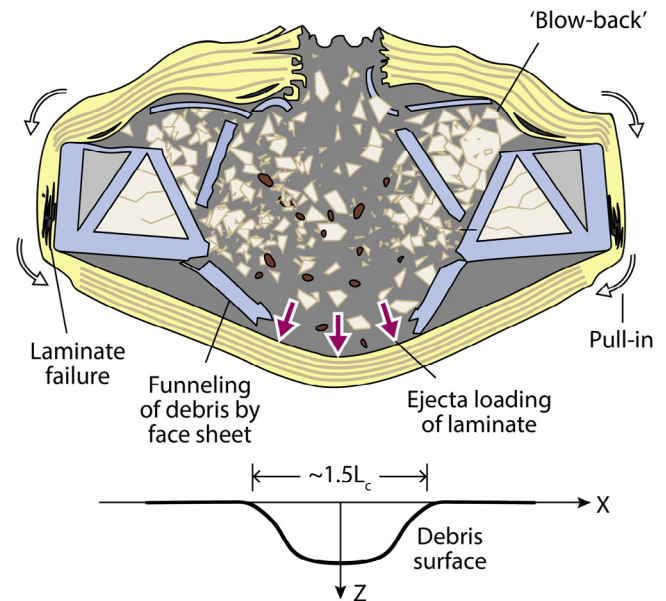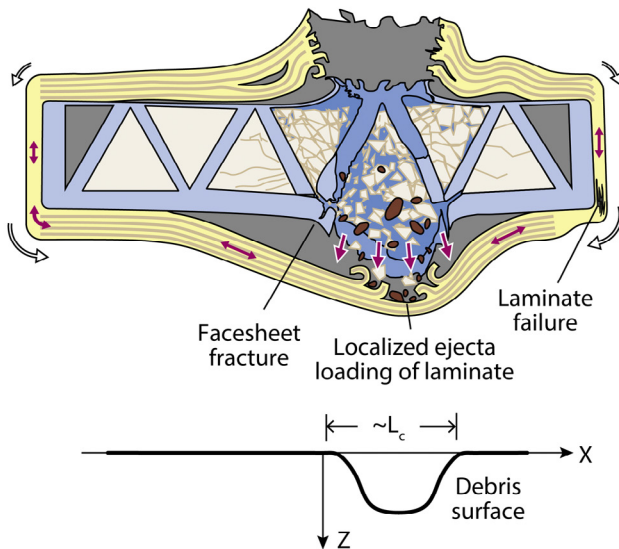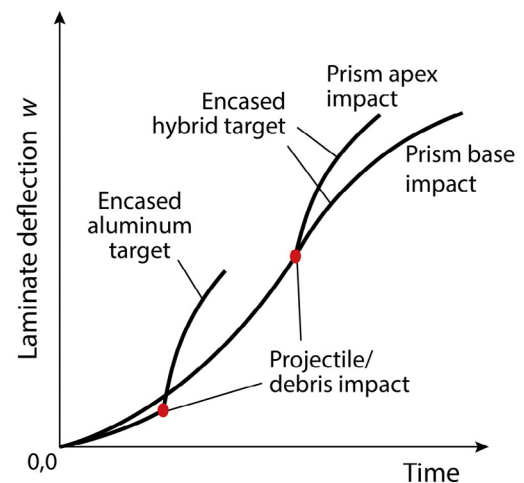
Fig. 17. Schematic illustration showing the loading sequence of the rear laminate of the encased hybrid target impacted on either (a–b) a prism base or (c) a prism apex. The rear laminate is (a) initially accelerated by the bulging rear face sheet and (b) subsequently impacted by the released debris fragments. (d) Proposed deflection history of the encased hybrid and encased aluminum targets both before and after impact by the debris/projectile.

This study has identified mechanisms which when activated increase the ballistic resistance of a laminate. Placement of a suitable material between the projectile and laminate can allow temporal and spatial modification of the material that impacts a laminate at the rear of the target. The use of the hybrid core sandwich panel here provided an effective means of activating projectile defeat by controlling the area of debris impacting the laminate backing. The study has not investigated the best hybrid sandwich structure design (e.g. face sheet thickness, web/face sheet nodal strength, cell topology and cell size), or material properties (e.g. density, yield strength, toughness and ductility), or the best ceramic type, dimensions, topology, etc. These would need to be considered in relation to the impactor (density, size, shape, velocity and obliquity of impact) and type of laminate backing. The study has shown

that laminate selection should address material indices that maximize both the usual membrane mode of action and the indirect tension mode of failure. It is finally noted that the laminate encasement method utilized here was of substantial benefit since it *i*) enabled the back, side and front portions of the laminate to all contribute to membrane stretching, and *ii*) eliminated stress concentrations at bolt hole attachments that would be otherwise necessary if a laminate plate was utilized as the spall shield.

6. Conclusions

The impact performance of an UHMWPE fiber reinforced polymer matrix composite (HB26 grade Dyneema®) has been studied using model test structures that enabled control of the spatial distribution

and velocity of ejecta. The Dyneema® laminate encased an aluminum alloy sandwich panel whose hybrid corrugated cores contained alumina prisms. It has been found that:

1. Self-gripping, Dyneema® encased targets were not penetrated when a 12.7 mm diameter hardened chrome steel sphere impacted the base of the center prism at a velocity $V_i \geq 2.7$ km s^{-1}. This corresponded to at least a 100% increase in the ballistic limit compared to a target that had the same laminate encasement and areal density, but used a solid aluminum plate to interact with the projectile.
2. Fragmenting, and spatially/temporally dispersing the momentum of the impact and pre-accelerating the rear Dyneema® laminate prior to debris impact combine to suppress local fiber failure and greatly increase the penetration resistance of the target.
3. Redistribution of the impact momentum by the hybrid core sandwich panel was controlled by ceramic fragmentation, nodal failures of the corrugated panel and bending of its face sheet. Targets impacted at a prism base were more effective at momentum redistribution than prism apex impacts (prism apex impacts resulted in perforation at $V_i = 2.50$ km s^{-1}). Pre-acceleration of the rear laminate by bulging of the rear face of the intervening panel reduced the debris impact velocity upon the rear laminate by at least 40%. This reduced the incident pressure upon the laminate, and probability of local penetration.
4. The kinetic energy of the debris plume exiting the hybrid core sandwich panel was dissipated by large deflection and membrane stretching of the full thickness laminate. The stress required for this has been reduced by engagement of Dyneema® at the sides and front of the encasement.

Acknowledgements

References

[1] O'Masta MR, Deshpande VS, Wadley HNG. Mechanisms of projectile penetration in Dyneema® encapsulated aluminum structures. Int J Impact Eng 2014;74:16–35. doi:10.1016/j.ijimpeng.2014.02.002.

[2] Hogg PJ. Composites in armor. Science 2006;314:1100–1. doi:10.1126/science.1131118.

[3] Fink BK. Performance metrics for composite integral armor. J Thermop Compos Mater 2000;13:417–31. doi:10.1106/FR0L-T33W-JPD0-VFH3.

[4] Vargas-Gonzalez LR, Walsh SM, Scott BR. Balancing ballistic and back-face deformation in helmets: the role of alternative resisns, fibers, and fiber architecture in mass-efficient head protection. In: Baker E, Templeton D, editors. Proceedings of the 26th international symposium on ballistics, vol. 2. Miami, FL: DEStech Publications, Inc.; 2011. p. 1872–82.

[5] Phoenix SL, Porwal PK. A new membrane model for the ballistic impact response and V50 performance of multi-ply fibrous systems. Int J Solid Struc 2003;40:6723–65. doi:10.1016/S0020-7683(03)00329-9.

[6] Karthikeyan K, Russell BP, Fleck NA, Wadley HNG, Deshpande VS. The effect of shear strength on the ballistic response of laminated composite plates. Eur J Mechan 2013;42:35–53. doi:10.1016/j.euromechsol.2013.04.002.

[7] Parsons EM, Weerasooriya T, Sarva S, Socrate S. Impact of woven fabric: experiments and mesostructure-based continuum-level simulations. J Mechan Phys Solid 2010;58:1995–2021. doi:10.1016/j.jmps.2010.05.006.

[8] Vargas-Gonzalez L, Walsh SM, Wolbert J. Impact and ballistic response of hybridized thermoplastic laminates. Aberdeen Proving Ground, MD: Army Research Laboratory. Technical Report ARL-MR-0769; 2011.

[9] Lee BL, Song JW, Ward JE. Failure of Spectra® Polyethylene fiber-reinforced composites under ballistic impact loading. J Compos Mater 1994;28:1202–26. doi:10.1177/002199839402801302.

[10] Chocron S, King N, Bigger R, Walker JD, Heisserer U, van der Werff H. Impacts and waves in Dyneema® HB80 strips and laminates. J Appl Mech 2013;80:doi:10.1115/1.4023349.

[11] Iremonger MJ. Polyethylene composites for protection against high velocity small arms bullets. In: Reinecke WG, editor. Proceedings of the 18th international symposium on ballistics. San Antonio, TX: Technomic Publishing Company, Inc; 1999. p. 946–54.

[12] Scott BR. The penetration of compliant laminates by compact projectiles. In: Reinecke WG, editor. Proceedings of the 18th international symposium on ballistics. San Antonio, TX: Technomic Publishing Company, Inc; 1999. p. 1184–91.

[13] Zhang Z, Shen S, Huancheng S, Zhang D. Ballistic penetration of dyneema fiber laminate. J Mater Sci Technol 1998;14:265–8.

[14] Grujicic M, Arakere G, He T, Bell WC, Cheeseman BA, Yen C-F, et al. A ballistic material model for cross-plied unidirectional ultra-high molecular-weight polyethylene fiber-reinforced armor-grade composites. Mater Sci Eng A-Struct: A 2008;498:231–41. doi:10.1016/j.msea.2008.07.056.

[15] Greenhalgh ES, Bloodworth VM, Iannucci L, Pope D. Fractographic observations on Dyneema® composites under ballistic impact. Compos Part A-Appl Sci Manuf 2013;44:51–62. doi:10.1016/j.compositesa.2012.08.012.

[16] Woodward RL, Egglestone GT, Baxter BJ, Challis K. Resistance to penetration and compression of fibre-reinforced composite materials. Compos Eng 1994;4:329–41. doi:10.1016/0961-9526(94)90083-3.

[17] Scott BR, Cheeseman BA. In: Bless S, Walker J, editors. The mechanics of projectile arrest for compliant cross plied unidirectional laminates, vol. 2. New Orleans, LA: DEStech Publications, Inc.; 2008.

[18] Heisserer U, van der Werff H, Hendrix J. Ballistic depth of penetration studies in Dyneema® composites. In: Wickert M, Salk M, editors. Proceedings of the 27th international symposium on ballistics, vol. 2. Freiburg, Germany: DEStech Publications, Inc.; 2013. p. 1936–43.

[19] Attwood JP, Khaderi SN, Karthikeyan K, Fleck NA, O'Masta MR, Wadley HNG, et al. The out-of-plane compressive response of composites. J Mechan Phys Solid 2014;doi:10.1016/j.jmps.2014.05.017.

[20] O'Masta MR, Deshpande VS, Wadley HNG. Defect controlled transverse compressive strength of polyethylene fiber laminates. Int J Solid Struc 2015;52:130–49. doi:10.1016/j.ijsolstr.2014.09.023.

[21] Chapman DJ, Braithwaite CH, Proud WG. The response of dyneema to shock-loading. AIP Conf Proc 2009;1195:1269–72. doi:10.1063/1.3295037.

[22] Hazell PJ, Appleby-Thomas GJ, Trinquant X, Chapman DJ. In-fiber shock propagation in Dyneema®. J Appl Phys 2011;110:doi:10.1063/1.3622294.

[23] Karthikeyan K, Russell BP. Polyethylene ballistic laminates: failure mechanics and interface effect. Mater Des 2014;63:115–25. doi:10.1016/j.matdes.2014.05.069.

[24] Cunniff PM. Dimensionless parameters for optimization of textile-based body armor systems. In: Reinecke WG, editor. Proceedings of the 18th international symposium on ballistics. San Antonio, TX: Technomic Publishing Company, Inc; 1999. p. 1303–10.

[25] Karthikeyan K, Russell BP, Fleck NA, O'Masta MR, Wadley HNG, Deshpande VS. The soft impact response of composite laminate beams. Int J Impact Eng 2013;60:24–36. doi:10.1016/j.ijimpeng.2013.04.002.

[26] Dehn JT. A unified theory of penetration. Aberdeen Proving Ground, MD: Ballistic Research Laboratory. Technical Report BRL-TR-2770; 1986.

[27] Yungwirth CJ, Radford DD, Aronson M, Wadley HNG. Experiment assessment of the ballistic response of composite pyramidal lattice truss structures. Compos Part B-Eng 2008;39:556–69. doi:10.1016/j.compositesb.2007.02.029.

[28] Yungwirth CJ, O'Connor J, Zakraysek A, Deshpande VS, Wadley HNG. Explorations of hybrid sandwich panel concepts for projectile impact mitigation. J Am Ceram Soc 2011;94:s62–75. doi:10.1111/j.1551-2916.2011.04501.x.

[29] Ni CY, Li YC, Xin FX, Jin F, Lu TJ. Ballistic resistance of hybrid-cored sandwich plates: numerical and experimental assessment. Compos Part A-Appl Sci Manuf 2013;46:69–79. doi:10.1016/j.compositesa.2012.07.019.

[30] Wadley HNG, Dharmasena KP, O'Masta MR, Wetzel JJ. Impact response of aluminum corrugated core sandwich panels. Int J Impact Eng 2013;62:114–28. doi:10.1016/j.ijimpeng.2013.06.005.

[31] Wadley HNG, O'Masta MR, Dharmasena KP, Compton BG, Gamble EA, Zok FW. Effect of core topology on projectile penetration in hybrid aluminum/alumina sandwich structures. Int J Impact Eng 2013;62:99–113. doi:10.1016/j.ijimpeng.2013.05.008.

[32] Russell BP, Karthikeyan K, Deshpande VS, Fleck NA. The high strain rate response of ultra high molecular-weight polyethylene: from fibre to laminate. Int J Impact Eng 2013;60:1–9. doi:10.1016/j.ijimpeng.2013.03.010.

[33] Schmidt TE, Tyson J, Galanulis K, Revilock DM, Melis ME. Full-field dynamic deformation and strain measurements using high-speed digital cameras. In: Paisley DL, Kleinfelder S, Snyder DR, Thompson BJ, editors. Proc. SPIE, vol. 5580. Alexandria, VA: 2005. p. 174–85. doi:10.1117/12.567142.

[34] Yu JH, Dehmer PG. Dynamic impact deformation analysis using high-speed cameras and ARAMIS photogrammetry software. Aberdeen Proving Ground, MD: Army Research Laboratory; 2010.

[35] Hisley DM, Gurganus JC, Drysdale AW. Experimental methodology using digital image correlation to assess ballistic helmet blunt trauma. Technical Report ARL-TR-52112. J Appl Mech 2011;78:051022. doi:10.1115/1.4004332.

[36] Compton BG, Gamble EA, Zok FW. Failure initiation during impact of metal spheres onto ceramic targets. Int J Impact Eng 2013;55:11–23. doi:10.1016/j.ijimpeng.2012.12.002.